Research in Astronomy and Astrophysics, 25:045006 (15pp), 2025 April
https://doi.org/10.1088/1674-4527/adc29c
CSTR: 32081.14.RAA.adc29c

Properties of Standard, Fuzzy, and Self-interacting Dark Matter Haloes in Dwarf Galaxies

Fahmi M. Al Farisy[1], Hesti R. T. Wulandari[2,3], and Azriel J. Dante[1]
[1] Master's Program in Astronomy, Faculty of Mathematics and Natural Sciences, Institut Teknologi Bandung, Bandung 40132, Indonesia
[2] Astronomy Research Division, Faculty of Mathematics and Natural Sciences, Institut Teknologi Bandung, Bandung 40132, Indonesia; h.wulandari@itb.ac.id
[3] Bosscha Observatory, Faculty of Mathematics and Natural Sciences, Institut Teknologi Bandung, Lembang 40391, Indonesia
Received 2024 September 10; revised 2025 March 11; accepted 2025 March 17; published 2025 April 8

Abstract

This study examines the properties of standard cold dark matter (CDM), fuzzy dark matter (FDM), and self-interacting dark matter (SIDM) haloes by analyzing the rotation curves of selected dwarf galaxies from SPARC and LITTLE THINGS in 3D catalogs. Utilizing the Markov Chain Monte Carlo (MCMC) method for model fitting and Bayesian Information Criterion for model comparison, we find that compared to CDM, both FDM and SIDM haloes generally provide better fits to the observed rotation curves. Our findings reveal that the concentration–mass relation derived from the dark matter-only simulations is not followed by concentrations or masses obtained from the rotation curve data. Our analysis highlights a positive correlation between the core sizes of FDM and SIDM haloes and the effective radius of the galaxy, attributable to gravitational couplings between baryonic and dark matter components. Moreover, our exploration of dark matter fractions at characteristic radii indicates considerable diversity in dark matter distributions across dwarf galaxies. Notably, FDM and SIDM exhibit greater diversity than CDM in this respect.

Key words: galaxies: dwarf – galaxies: kinematics and dynamics – galaxies: haloes – (cosmology:) dark matter

1. Introduction

In modern cosmology, cold dark matter (CDM) is widely accepted as the dominant matter component of the universe. Indications of the need for dark matter range from galactic scales, as shown by non-declining rotation curves of spiral galaxies (Rubin & Ford 1970; Rubin et al. 1978; Persic et al. 1996; Sofue et al. 1999), to cosmological scales, including large-scale structures (see Springel et al. 2005; Angulo & Hahn 2022 and references therein) and the cosmic microwave background (CMB; Bennett et al. 2013; Planck Collaboration 2020). CDM is assumed to be non-relativistic, collisionless (interacts only through gravity), and dissipationless (does not lose energy through radiation). This CDM paradigm is crucial for understanding cosmic evolution and structure formation.

Despite support from many observational results, the CDM scenario suffers from several small-scale problems. These problems are related to the distribution of dark matter in the central haloes and properties of dwarf galaxies (Bullock & Boylan-Kolchin 2017; Sales et al. 2022), such as the missing satellite problem (MSP), core-cusp problem (CCP), and diversity problem. The MSP relates to cosmological simulations with the CDM model that predict galaxies like the Milky Way have at least one order higher dwarf galaxies than observed (Klypin et al. 1999; Moore et al. 1999). The CCP is associated with the dark matter density at the inner halo radius of dwarf and low surface brightness (LSB) galaxies that tends to flatten (cored) rather than increase toward the center (cuspy) following the $\rho \propto 1/r$ relation (Navarro et al. 1996, 1997) as in the CDM simulations (Flores & Primack 1994; Moore 1994; Oh et al. 2015; Li et al. 2020). The diversity problem refers to the heterogeneity in the shapes of rotation curves observed in the inner radius of galaxies of similar mass, contradictory to CDM simulations that suggest self-similarity (Oman et al. 2015; Del Popolo et al. 2018; Zentner et al. 2022), i.e., haloes of the same mass should exhibit similar rotation curves.

To overcome the problems of CDM on galaxy scales, several solutions have been proposed. One of them is by incorporating baryonic processes into the CDM model. Baryonic inflows and outflows during galaxy formation may change the inner dark matter profiles: cores are created by baryonic blowouts (Navarro et al. 1996; Pontzen & Governato 2012; Di Cintio et al. 2014), but cusps can be recreated by further baryonic infall (Tollet et al. 2016; Benítez-Llambay et al. 2019). Santos-Santos et al. (2020) found that the rotation curve shape correlates with baryonic surface density: high surface density galaxies exhibit rapidly rising rotation curves consistent with cuspy CDM haloes, while low surface density galaxies show slowly rising curves indicative of inner mass deficits or "cores." However, the correlation appears too weak to solely drive the diversity in the shapes of rotation curves.

Another way to address small-scale problems is to propose alternative models that modify or extend the assumptions of

CDM. These alternatives aim at explaining the observed discrepancies in the behavior of dark matter at smaller scales while retaining the successes of the standard CDM framework on the cosmological scales (Bullock & Boylan-Kolchin 2017; Del Popolo et al. 2018; de Martino et al. 2020). Among alternative models to the standard CDM are fuzzy dark matter (FDM) and self-interacting dark matter (SIDM), which will be the focus of this paper.

FDM is composed of ultra-light axion particles with a mass range of 10^{-24}–10^{-19} eV (Hu et al. 2000; Matos & Arturo Ureña-López 2001; Schive et al. 2014a). On scales comparable to the de Broglie wavelength λ_{dB} of FDM particles (order of kpc), quantum pressure balances gravitational forces, leading to the formation of a solitonic core with a constant density of a typical size of $\sim$1 kpc (Marsh & Pop 2015; Mocz et al. 2019; de Martino et al. 2020; May & Springel 2021). The constant-density core transitioning to a CDM-like distribution in the outer halo (Schive et al. 2014a; Veltmaat et al. 2018; Mocz et al. 2019; Mina et al. 2022) suggests that FDM can solve the CCP. In addition to preventing the formation of cusps, quantum pressure can also suppress the formation of structures smaller than dλ_{dB}, indicated by a cutoff in the power spectrum of the FDM halo (Matos & Arturo Ureña-López 2001; Schive et al. 2014a). For typical masses of FDM particles that have been studied, $m_{\rm FDM} \approx 10^{-22} M_{\odot}$, this cutoff occurs in haloes with masses $<10^{8} M_{\odot}$, which form abundantly in CDM simulations (Ferreira 2021). Therefore, FDM has also been suggested as a solution to the problem of missing satellites.

In the SIDM model, dark matter particles interact with each other non-gravitationally through strong or weak forces, involving the exchange of mediator particles (Spergel & Steinhardt 2000; Tulin & Yu 2018). SIDM particles behave like collisionless CDM at larger scales, where the collision rate is negligible due to the smaller density. SIDM models are generally characterized by the value of the scattering cross-section per unit mass σ/m_{χ}, with typical values of $\sim$1–10 cm^2 g^{-1} for galaxy scales (de Martino et al. 2020; Kaplinghat et al. 2020; Zentner et al. 2022). Cosmological simulations with SIDM models show that the interactions between dark matter particles allow for thermalization processes that lead to the transfer of energy and momentum from the inner radius to the outer radius of the halo (Rocha et al. 2013; Tulin & Yu 2018). This kind of process results in the formation of a constant density isothermal core that depends on the value of σ/m_{χ} (Correa 2023; Rocha et al. 2013). Therefore, SIDM can be an alternative solution to the CCP. The thermalization processes also "bind" the distribution of dark matter and baryons in the inner radius of the halo, which means the size of the isothermal dark matter core and the shape of its density profile depend on the baryon distribution (Ren et al. 2019). This allows the SIDM halo model to fit both cored profiles in galaxies with low baryon concentrations such as dwarf and LSB galaxies, and cuspy profiles in galaxies with high baryon concentrations such as massive and high surface brightness (HSB) galaxies (Vogelsberger et al. 2014; Despali et al. 2019; Zentner et al. 2022). Hence, SIDM offers a potential solution to the problem of rotation curve diversity.

In this study, we test three dark matter models: standard CDM, FDM, and SIDM using dwarf galaxy rotation curve data from SPARC (Lelli et al. 2016) and LITTLE THINGS in 3D (Iorio et al. 2017), hereafter referred to as LT in 3D. Previous research predominantly focuses on testing FDM (Bar et al. 2018, 2022; Bernal et al. 2018; Bañares-Hernández et al. 2023; Khelashvili et al. 2023) and SIDM (Ren et al. 2019; Kaplinghat et al. 2020; Loizeau & Farrar 2021; Zentner et al. 2022) models separately, usually utilizing a single dataset, commonly from SPARC. By incorporating the LT in 3D catalog, our study extends the data range to lower mass galaxies, enabling a more comprehensive examination of the influence of galaxy physical parameters on the fit to alternative dark matter models. Furthermore, by evaluating both FDM and SIDM models within a single study, we aim to compare distinct features of the two models in the rotation curves. While most studies of halo properties rely on cosmological simulations (Rocha et al. 2013; Schive et al. 2014a; Vogelsberger et al. 2014; Marsh & Pop 2015; Creasey et al. 2017), our approach differs as we derive halo properties such as the concentration–mass relation, core size, and dark matter fraction directly from rotation curve data and compare these with results of existing cosmological simulations. We organize the paper as follows: Section 2 outlines the data utilized in this study, in Section 3 the rotation curve fitting method is explained, results are presented and compared with simulations in Sections 4 and 5, and finally, we present our conclusions in Section 6. Throughout this work, we adopt the Planck cosmology with $H_0 = 67.8$ km s^{-1} Mpc^{-1} (Planck Collaboration 2020).

2. Data

Both the SPARC (Lelli et al. 2016) and LT in 3D (Iorio et al. 2017) catalogs provide photometric data in 3.6 μm and rotation curves. The SPARC catalog includes rotation curves of 175 late-type galaxies with stellar masses of $7.477 \lesssim \log M_{*}(M_{\odot}) \lesssim 11.477$. Mass models for the stellar disk, bulge, and gas disk components are available in SPARC, assuming a mass-to-light ratio of 1 for both the disk and bulge components. This value of mass-to-light ratio should be adjusted in the Markov Chain Monte Carlo (MCMC) fitting process of each galaxy.

The LITTLE THINGS catalog originally contained rotation curve data of 26 Local Group dwarf irregular galaxies with $5.602 \lesssim \log M_{*}(M_{\odot}) \lesssim 9.309$ (Oh et al. 2015). Iorio et al. (2017) reselected the galaxies and redetermined their rotation curves using the 3D method with 3D-Barolo (Di Teodoro & Fraternali 2015), and the results are dubbed LITTLE THINGS in 3D, which includes 17 galaxies. The velocity data in LT in 3D consist of circular rotation speeds corrected for pressure support from the random motion of the gas. Some galaxies are

marked as "rogue" due to their very small or very large inclinations (inclination rogues), large distance uncertainties (distance rogues), or system disequilibrium (disequilibrium rogues) (Bañares-Hernández et al. 2023), which make the resulting rotation curves less reliable. The galaxy parameter data in LT in 3D are taken from Read et al. (2017).

In this study, we focus on dwarf galaxies ($M_* \leqslant 10^{10} M_\odot$) and include only those whose inclinations are in the range of $30^\circ \leqslant i \leqslant 75^\circ$. We select high-quality rotation curves, i.e., those with the highest quality flag parameter (QF = 1) in the SPARC catalog and not classified as distance rogues or disequilibrium rogues in the LT in 3D catalog. We also ensure that each rotation curve has a minimum of seven data points with the innermost observation point at a radius of less than 0.5 kpc. Using these selection criteria, we obtain a final sample of 39 galaxies (27 SPARC galaxies and 12 LT in 3D galaxies).

3. Methodology

3.1. Dark Matter Halo Models

3.1.1. NFW Mass Model

The standard CDM halo can be well described by Navarro–Frenk–White (NFW) profiles derived from dark matter-only N-body simulations (Navarro et al. 1996, 1997),

$$\rho_{\rm NFW} = \frac{\rho_n}{\left(\frac{r}{r_n}\right)\left(1+\left(\frac{r}{r_n}\right)\right)^2}, \tag{1}$$

where r is the radial distance from the halo center, ρ_n denotes the density at the halo center, and r_n is the scale radius.

Although ρ_n and r_n are natural parametrizations of the NFW density profile, their values can vary significantly across galaxies. Therefore, following Li et al. (2020), we use the rotation velocity and concentration parameter at r_{200}, denoted respectively as V_{200} and C_{200}, as free fitting parameters (see Section 3.3). The characteristic radius r_{200} encloses a region with an average density of 200 times the critical density of the universe. The velocity V_{200} is given by

$$V_{200}^2 = \frac{G}{r_{200}} \int_0^{r_{200}} 4\pi r \rho_{\rm DM} r^2 dr, \tag{2}$$

and the concentration parameter is defined as

$$C_{200} = \frac{r_{200}}{r_n}. \tag{3}$$

In this work, we also test the concentration–mass relation for the NFW model obtained from cosmological simulations by Dutton & Macciò (2014),

$$\log C_{200,\rm NFW} = 0.905 - 0.101 \log(M_{200}/[10^{12} h^{-1} M_\odot]), \tag{4}$$

which has an original scatter of 0.11 dex. However, we follow Bañares-Hernández et al. (2023) and use a more conservative scatter of 0.16 dex.

3.1.2. FDM Mass Model

The evolution of FDM halo can be described by the time-dependent Schrödinger–Poisson equations (Hu et al. 2000)

$$i\hbar \frac{\partial \psi}{\partial t} = -\frac{\hbar^2}{2m} \nabla^2 \psi + mV\psi, \tag{5a}$$

$$\nabla^2 V = 4\pi G \rho_d, \tag{5b}$$

where $\hbar$ denotes the reduced Planck constant, ψ is the wave function, $\rho_d = m|\psi|^2$ designates the density of dark matter, and V is the self-gravitational potential of dark matter.

The density profile of the FDM halo is empirically derived from cosmological simulations of the FDM model (Schive et al. 2014a), and can be divided into two regions: the inner soliton core and the outer NFW-like structure separated by a transition radius r_a,

$$\rho_{\rm FDM}(r) = \begin{cases} \rho_{\rm sol}(r), & r \leqslant r_a, \\ \rho_{\rm NFW}(r), & r \geqslant r_a. \end{cases} \tag{6}$$

The division of the profiles is motivated by the prediction that FDM will lose its wave phase coherence at large distances from the center of the matter distribution, so that there will be a transition from the soliton profile to the NFW profile at increasingly large radii (Marsh & Pop 2015).

The soliton core density distribution is described by the ground state "boson-star" solution of Equation (5a) (Schive et al. 2014a, 2014b),

$$\rho_{\rm sol}(r) = \frac{\rho_{\rm sol,0}}{\left(0.091\left(\frac{r}{r_{\rm sol}}\right)^2\right)^8}, \tag{7}$$

with $\rho_{\rm sol,0}$ and $r_{\rm sol}$ respectively denoting the central density and radius of the soliton (Schive et al. 2014a). The value of $r_a = \alpha r_{\rm sol}$ with $\alpha \approx 3$ (Schive et al. 2014a; Mina et al. 2022) is not universal for all dark matter haloes (Khelashvili et al. 2023).

The relation between $\rho_{\rm sol,0}$, $r_{\rm sol}$, and FDM particle mass ($m_{\rm FDM} = m_{22} \times 10^{-22}$ eV) is given by Schive et al. (2014a)

$$\rho_{\rm sol,0} = \frac{0.019}{m_{22}^2 \left(\frac{r_{\rm sol}}{\rm kpc}\right)^4} \frac{M_\odot}{\rm pc^3}. \tag{8}$$

We also consider the scaling relation between the soliton core mass ($M_{\rm sol}$) and halo virial mass ($M_{\rm vir}$) (Schive et al. 2014b; Hui et al. 2017),

$$M_{\rm sol} = 2.7 \times 10^8 \frac{\delta}{m_{22}} \left(\frac{M_{\rm vir}}{10^{10} M_\odot}\right)^{1/3} M_\odot. \tag{9}$$

The factor δ expresses the scatter or uncertainty of this relation.

In general, the FDM profile can be described by four parameters: ρ_s and r_s for the soliton core, r_a for the profile transition radius, and r_n for the NFW tail. The NFW parameter ρ_n is set by the continuity condition. Following Khelashvili et al. (2023), we use

the logarithm of the FDM particle mass, $\log m_{22}$, the ratio between the transition and soliton radii $\alpha = r_a/r_s$, the parameter δ (see Equation (9)) and the rotational velocity V_{200} as free parameters. Those parameters could be translated directly into ρ_s, r_s, ρ_n, and r_n through the relations in Equations (8) and (9).

The FDM halo velocity parameterization is obtained following Khelashvili et al. (2023). The density profile of the soliton core and NFW halo in the FDM model can be written respectively as

$$\rho_{\rm sol}(r) = \rho_{\rm sol,0}\, f_{\rm sol}\,(r/r_{\rm sol}), \tag{10a}$$

$$\rho_{\rm NFW}(r) = \rho_s f_{\rm NFW}\,(r/r_s), \tag{10b}$$

with

$$f_{\rm sol}\,(x) = \frac{1}{(1 + 0.091 \cdot x^2)^8}, \quad x = r/r_{\rm sol}, \tag{11a}$$

$$f_{\rm sol}\,(x) = \frac{1}{x(1+x)^2}, \quad x = r/r_s. \tag{11b}$$

The rotational velocity profile of the FDM halo can be stated as

$$V_{\rm FDM}(x) = V_{200}\sqrt{\frac{C_{200}}{x}\frac{\mu(x)}{\mu(C_{200})}}, \tag{12}$$

with

$$\mu(x) = I_{\rm sol}(\min[\alpha, x]) + KI_{\rm NFW}\left(\frac{\alpha}{\beta}, \frac{x}{\beta}\right). \tag{13}$$

Equation (13) is an auxiliary function that connects the soliton core profile in the inner region with the NFW profile in the outer region. The parameters $\alpha = r_a/r_{\rm sol}$, $\beta = r_s/r_{\rm sol}$, and $K = \beta^6 f_{\rm sol}^2$ are obtained from the density continuity condition at the transition radius, while $I_{\rm sol}$ and $I_{\rm NFW}$ represent the mass of dark matter enclosed within radius r and are given respectively by

$$I_{\rm sol}(x) = \int_0^x x'^2 f_{\rm sol}\,(x')\,dx', \tag{14a}$$

$$I_{\rm NFW}(x_1; x_2) = \max\left[0, \int_{x_1}^{x_2} x'^2\, f_{\rm NFW}(x')\,dx'\right]. \tag{14b}$$

Equation (14a) can be integrated numerically to obtain respectively

$$\begin{aligned} I_{\rm sol}(u) = \tfrac{1}{a}[&3465(u^{13} - u + (u^2+1)^7 \arctan(u)) \\ &+ 23100u^{11} + 65373u^9 + 101376u^7 \\ &+ 92323u^5 + 48580u^3], \end{aligned} \tag{15a}$$

$$\begin{aligned} &I_{\rm NFW}(x_1; x_2) \\ &= \max\left[0, \ln\frac{|x_2+1|}{|x_1+1|} + \frac{1}{|x_2+1|} - \frac{1}{|x_1+1|}\right], \end{aligned} \tag{15b}$$

with $u = \sqrt{0.091}\,x^2$ and $a = 0.091^{3/2} \cdot 215040\,(u^2+1)^7$.

Assuming a spherically symmetric halo, C_{200} can be expressed as

$$C_{200} = \frac{0.0537 m_{22}\delta V_{200}^2 \rho_{\rm crit}^{1/3}}{H_0^2}, \tag{16}$$

and

$$\mu(C_{200}) = \frac{0.350877 m_{22}^2 \delta V_{200}^4 \rho_{\rm crit}}{C_{200} H_0^4}. \tag{17}$$

Equation (16) allows C_{200} to be expressed in terms of the free parameters of the FDM halo model, while Equation (17) is solved numerically by a direct iteration method (see Appendix A7 in Karttunen et al. 2017) to find the value of β.

We also examine the concentration–mass relation of the FDM model (Dentler et al. 2022; Bañares-Hernández et al. 2023),

$$\begin{aligned} C_{200,\rm FDM} = &\left(1 + \left(15 \cdot \left(\frac{1.6 \times 10^{10} \cdot (10^{\log m_{22}})^{-4/3}}{M_{200}}\right)\right)\right)^{-0.3} \\ &\cdot C_{200,\rm NFW}, \end{aligned} \tag{18}$$

with $C_{200,\rm NFW}$ given by Equation (4).

3.1.3. SIDM Mass Model

The SIDM density profile is modeled with the analytical Jeans isothermal approach (Kaplinghat et al. 2014, 2016; Zentner et al. 2022), which has been verified with numerical simulations of an isolated SIDM halo (Creasey et al. 2017). The SIDM halo is divided into the inner and outer regions separated by a characteristic radius r_1. This radius is defined as the point at which SIDM particles, on average, experience at least one interaction throughout the halo's age ($t_{\rm age}$). SIDM interparticle scatterings are rare in the outer regions, allowing the halo distribution to be effectively modeled using the NFW profile. In contrast, in the inner regions, the SIDM halo has been thermalized, allowing its distribution to be well modeled by an isothermal profile,

$$\rho_{\rm ISO}(r) = \rho_0 \exp\left(-\frac{\Delta\Phi_{\rm tot}(r)}{\sigma_{v0}^2}\right), \tag{19}$$

where $\Delta\Phi_{\rm tot}(r) = \Phi_{\rm tot}(r) - \Phi_{\rm tot}(0)$ denotes the difference between the total gravitational potential at radius r and the total gravitational potential at the center. This formula accounts for contributions from the isothermal halo and baryonic matter, assuming spherical symmetry in the mass distribution. Here ρ_0 represents the central density of the SIDM halo, while σ_{v0} denotes the one-dimensional velocity dispersion of SIDM particles. The density profile of the SIDM halo is characterized by an isothermal profile in the inner region and an NFW profile in the outer region. These two profiles are connected at the transition point r_1 such that the SIDM density and mass

enclosed are continuous at this point,

$$\rho_{\rm SIDM}(r) = \begin{cases} \rho_{\rm ISO}(r) & \text{if } r \leqslant r_1, \\ \rho_{\rm NFW}(r) & \text{if } r \geqslant r_1. \end{cases} \quad (20)$$

The value of r_1 can be determined from the relation

$$\left\langle \frac{\sigma v_{\rm rel}}{m_\chi} \right\rangle \rho_{\rm SIDM}(r_1) t_{\rm age} \approx 1, \quad (21)$$

where σ denotes the scattering cross-section, $v_{\rm rel}$ is the relative scattering velocity between SIDM particles, m_χ is the mass of SIDM particles, $\rho_{\rm SIDM}(r_1)$ is the density of the SIDM halo at radius r_1, and the symbol $\langle \ldots \rangle$ indicates the average values of the parameters over the Maxwellian velocity distribution.

For dwarf galaxies or LSB galaxies, a cross-section of $\sigma/m_\chi = 3\,{\rm cm^2\,g^{-1}}$ is preferred (Kamada et al. 2017; Ren et al. 2019). In contrast, clusters favor smaller values such as $\sigma/m_\chi < 1\,{\rm cm^2\,g^{-1}}$ (Sagunski et al. 2021), which are insufficient to form cores in dwarf galaxies (Rocha et al. 2013; Zavala et al. 2013). Velocity-dependent models have been proposed to allow the cross-section to vary with relative velocity (Correa 2023). However, Zentner et al. (2022) showed that on typical galaxy scales, velocity dependence is unlikely to vary significantly. Thus, we assume the cross-section is independent of $v_{\rm rel}$ in our analysis and express the average scattering term as $\left\langle \frac{\sigma v_{\rm rel}}{m_\chi} \right\rangle = \frac{\sigma}{m_\chi}\left(\frac{4}{\sqrt{\pi}}\right)\sigma_{v_0}$.

For a given baryon density profile, $\rho_{\rm b}(r)$, the isothermal density profile can be derived using Equations (20) and (21), along with the Poisson equation

$$\nabla^2 \Phi_{\rm tot}(r) = 4\pi G[\rho_{\rm ISO}(r) + \rho_{\rm b}(r)], \quad (22)$$

which explicitly shows how the isothermal profile depends on the baryon density profile. Self-interactions among dark matter particles facilitate efficient heat transfer in the central regions of dark matter haloes, leading to the formation of an isothermal core with a flattened density profile and thermal equilibrium (Kamada et al. 2017). When baryons dominate the gravitational potential, they deepen the potential well, causing dark matter to adopt a more compact configuration. The thermal coupling between baryons and dark matter amplifies this effect by redistributing energy from baryonic processes more effectively through dark matter collisions (Kaplinghat et al. 2014; Vogelsberger et al. 2014).

To determine the baryon density profile, $\rho_b(r)$, we first need to reconstruct the baryon mass profile, $M_b(\leqslant r)$, by using the following equation,

$$M_b(\leqslant r_i) = \frac{[\Upsilon_* V^2_{\rm disk}(r_i) + V^2_{\rm gas}(r_i)]\, r_i}{G}, \quad (23)$$

where r_i denotes the radius of the ith observational data point, Υ_* symbolizes stellar mass-to-light ratio, and $V_{\rm disk}$ and $V_{\rm gas}$ are the rotational velocities of the disk and gas components respectively. We assume that the baryon distribution is spherically symmetric. For LT in 3D galaxies, Υ_* is already included in $V_{\rm disk}$. The function $M_b(\leqslant r)$ can be approximated by performing a quadratic interpolation between two consecutive observational data points within the radial range of the innermost radius ($r_{\rm min}$) and the outermost radius ($r_{\rm max}$) to ensure the baryon density profile (ρ_b) is smooth and continuous. Then, following Zentner et al. (2022), ρ_b can be approximated as

$$\rho_b(r) = \begin{cases} M_b(r_{\rm min})/(4\pi r^3_{\rm min}/3), & r < r_{\rm min}, \\ (dM_b(r)/dr)/(4\pi r^2), & r_{\rm min} \leqslant r \leqslant r_{\rm max}, \\ \rho_b(r_{\rm max})/(r_{\rm max}/r)^4, & r > r_{\rm max}. \end{cases} \quad (24)$$

Equation (19) can be rewritten as

$$\Phi_{\rm tot}(r) - \Phi_{\rm tot}(0) = -\sigma^2_{v0}[\ln\rho_{\rm ISO}(r) - \ln\rho_0]. \quad (25)$$

By applying the Poisson equation to both sides of Equation (25) and recalling that $\Phi_{\rm tot} = \Phi_{\rm ISO} + \Phi_{\rm b}$, we rewrite Equation (22) as

$$\frac{1}{r^2}\frac{d}{dr}\left(r^2 \frac{d}{dr}\ln\rho_{\rm ISO}(r)\right) = -\frac{4\pi G}{\sigma^2_{v0}}[\rho_{\rm ISO}(r) + \rho_{\rm b}(r)]. \quad (26)$$

The isothermal density profile, $\rho_{\rm ISO}(r)$, can be constructed by solving Equation (26). Following the methodology outlined by Ren et al. (2019), the calculation starts from 10% of the innermost radius of the rotation curve data. This approach is based on the assumption of a flat isothermal halo profile in the central region, which is represented by the condition $\frac{1}{r}\frac{d\rho_{\rm ISO}}{dr} = \frac{d\ln\rho_{\rm ISO}}{dr} = 0$. The integration of $\rho_{\rm ISO}(r)$ is performed outwards from this initial radius up to $n \times r_{\rm max}$, where the number n varies from galaxy to galaxy, and $r_{\rm max}$ is the outermost radius of the rotation curve. The value of $n \times r_{\rm max}$ is adjusted to satisfy the condition that $n \times r_{\rm max} > r_1$.

The halo density at the transition radius, $\rho_{\rm SIDM}(r_1)$, is calculated using Equation (21), and the transition radius r_1 can be obtained from the constructed isothermal density profile. We set the SIDM particle scattering rate,

$$\Gamma_0 = \rho_0\left(\frac{\sigma}{m_\chi}\right)\frac{4}{\sqrt{\pi}}\sigma_{v0}, \quad (27)$$

as a fitting parameter along with the velocity dispersion σ_{v0}. We assume a halo age of $t_{\rm age} = 10$ Gyr and a value of $\sigma/m_\chi = 3\,{\rm cm^2\,g^{-1}}$, which are good approximations for the scale of dwarf galaxies (Ren et al. 2019; Zentner et al. 2022).

To construct the NFW density profile in the outer region ($r > r_1$), we employ the direct iteration numerical method (see Appendix A7 in Karttunen et al. 2017). This approach allows us to obtain the NFW halo parameters (ρ_n and r_n) from the density and mass continuity equations of the isothermal and

NFW halo at r_1,

$$\rho_{\rm ISO}(r_1) = \frac{\rho_n r_s^3}{r_1(r_n + r_1)^2}, \tag{28a}$$

$$4\pi \int_0^{r_i} (r')^2 \rho_{\rm ISO}(r') dr' = 4\pi\rho_n r_n^3 \left[\ln\left(1 + \frac{r_1}{r_n}\right) - \frac{r_1}{r_n + r_1} \right]. \tag{28b}$$

The SIDM halo mass profile can then be calculated after constructing the SIDM halo density profile, which is a combination of isothermal and NFW profiles,

$$M_{\rm SIDM}(<r) = \begin{cases} 4\pi \int_0^r (r')^2 \rho_{\rm ISO}(r') dr' & r < r_1, \\ M_{\rm SIDM}(\leqslant r_1) + M_{\rm NFW}(\leqslant r) - M_{\rm NFW}(\leqslant r_1) & r > r_1. \end{cases} \tag{29}$$

3.2. Rotational Velocity Model

We use the rotational velocity model from Li et al. (2020). The total rotational velocity $v_{\rm tot}$ is the sum of the contributions of baryons (stellar disk and gas) and the dark matter halo,

$$v_{\rm tot}^2 = |v_{\rm gas}| v_{\rm gas} + \Upsilon_* |v_{\rm disk}| v_{\rm disk} + v_{\rm DM}^2, \tag{30}$$

where Υ_* is the mass-to-light ratio of the stellar disk.

For SPARC galaxies, the baryonic mass is modeled using the stellar disk and gas models given by Lelli et al. (2016). Meanwhile, for LT in 3D galaxies, the baryon contribution is determined by employing the exponential disk model (Freeman 1970; Persic & Salucci 1990), utilizing parameters from Read et al. (2017). Since both SPARC and LT in 3D use photometric data at the same wavelength, they can be treated equally.

The rotational velocity of the dark matter component is determined through a fitting process assuming a spherically symmetric halo. Knowing the dark matter mass enclosed by radius r,

$$M_{\rm DM}(\leqslant r) = 4\pi \int_0^r r'^2 \rho_{\rm DM}(r')\, dr', \tag{31}$$

the rotational velocity profile of the dark matter halo is obtained from

$$V_{\rm DM}(\leqslant r) = \sqrt{\frac{G M_{\rm DM}(\leqslant r)}{r}} = \sqrt{\frac{4\pi G}{r} \int_0^r r'^2 \rho_{\rm DM}(r')\, dr'}. \tag{32}$$

3.3. Data Analysis

We apply Bayesian inference to constrain the model parameters. According to Bayes' theorem, the posterior probability density of the parameter θ given the data D and model M is

$$P(\theta|D, \mathcal{M}) = \frac{P(D|\theta, \mathcal{M})\pi(\theta|\mathcal{M})}{P(D|\mathcal{M})}, \tag{33}$$

where $P(D|\theta, \mathcal{M})$ is the likelihood of the data D given the parameter θ and model M, $\pi(\theta|\mathcal{M})$ is the prior probability density of the parameter θ given model M, and $P(D|\mathcal{M})$ is the evidence or marginal likelihood of the data under model M. We assume that the likelihood function is Gaussian,

$$P(D|\theta, \mathcal{M}) = \prod_i \frac{1}{\sqrt{2\pi\sigma_i}} \exp\left(-\frac{(v_{i,\rm obs} - v_{\rm pred}(\theta, \mathcal{M})(r_i))^2}{2\sigma_i^2} \right), \tag{34}$$

where $v_{i,\rm obs}$ and σ_i are the observed rotational velocity at radius r_i and its uncertainty respectively, and $v_{\rm pred}(\theta, \mathcal{M})(r)$ is the predicted rotational velocity calculated from model $\mathcal{M}$ given the parameter θ.

We utilize the Python library `emcee` (Goodman & Weare 2010; Foreman-Mackey et al. 2013) for our MCMC simulations. Table 1 lists the priors for each parameter. The convergence of the MCMC chains is monitored through the autocorrelation time, which indicates the number of iterations needed to yield effectively independent samples. To ensure reliable convergence and robust sampling, we set the number of MCMC iterations to at least 50 times the estimated autocorrelation time.

In this analysis, the value of maximum a posteriori (MAP) and the 95% credible interval of the posterior distribution will be assigned as the value of each parameter and the range of its uncertainties. The MAP value is defined as the parameter value that produces the maximum posterior probability, which can mathematically be written as

$$\hat{\theta}_{\rm MAP} = \arg\max_{\theta} [\ln P(\theta|d, \mathcal{M})]. \tag{35}$$

Meanwhile, the 95% credible interval is calculated using the highest posterior density interval (HPDI) with $\alpha = 0.95$, following the work of Khelashvili et al. (2023).

4. Results

4.1. Model Comparison

Statistical tests are required for performance comparison of different models in fitting data. In several studies, including those by Ren et al. (2019), Kaplinghat et al. (2020), and Li et al. (2020), the reduced chi-squared test has been employed to compare models fitted to the SPARC galaxy sample. A model is more favorable if it yields more galaxies with reduced chi-squared values approaching 1, indicating a good fit. However, it is crucial to recognize that the goodness-of-fit analysis using reduced chi-squared values can be misleading due to various factors that may influence these values beyond mere fitting quality. For instance, overestimated errors in data points and

Table 1
MCMC Priors for Free Parameters of the Three Different Halo Models

Parameter	Model	Fiducial	Unit	Range	Prior	Scatter
V_{200}	NFW, FDM	⋯	km s^{-1}	10–500	uniform	
C_{200}	NFW, FDM	⋯	⋯	>0	(4), (18)	$\sigma = 0.16$ dex
m_{22}	FDM	⋯	⋯	10^{-3}–10^{3}	log-uniform	
α	FDM	3	⋯	1–7	uniform	
δ	FDM	1	⋯	0.5–1.5	log-uniform	
Γ_0	SIDM	⋯	0.1 Gyr^{-1}	$\log_{10} 2 - 5$	uniform	
σ_{v0}	SIDM	⋯	km s^{-1}	2–100	uniform	
Υ_*	All (SPARC)	0.5	$\Upsilon_\odot$	⋯	normal	$\sigma = 0.11$ dex
M_*	All (LT in 3D)	(Read et al. 2017)	$M_\odot$	⋯	log-normal	$\sigma = \frac{1}{2}\log \frac{\delta_{M_{*0}+\delta_{M_{*+}}}}{\delta_{M_{*0}-\delta_{M_{*-}}}}$ dex

numerous fitting parameters can skew results. More complex models, while potentially offering better fits, possess greater flexibility, which can lead to overfitting. In addition, commonly used degree-of-freedom calculations may not apply to nonlinear models such as the dark matter halo model (Andrae et al. 2010; Zentner et al. 2022). This limitation underscores the need for careful consideration when interpreting reduced chi-squared values, as they may not fully capture the intricacies of model performance in all scenarios.

To address the limitation of the reduced chi-squared test, we employ the Bayesian Information Criterion (BIC), which is a more robust framework for model comparison. BIC evaluates a model's goodness of fit while penalizing the number of parameters. The BIC value is calculated from the following formula,

$$\mathrm{BIC} = -2 \cdot \ln(L) + k \cdot \ln(N), \tag{36}$$

where L represents the maximum likelihood of the model, k denotes the number of free parameters in the model (reflecting the complexity of the model), and N is the number of data points used in fitting the model. A lower BIC value indicates a better model fit when comparing multiple models, taking both model accuracy and simplicity into account.

The BIC analysis indicates that the SIDM model outperforms the other models analyzed, attaining the lowest BIC values for 23 galaxies, followed by the FDM model with 12 galaxies, and the NFW model with only three galaxies. Despite the FDM halo model generally giving favorable reduced chi-squared values, it does not emerge as the best model for most galaxies. This is mainly due to its higher number of fitting parameters, which can result in overfitting.

For each galaxy in the sample, we calculate the difference in the BIC values between two distinct models,

$$\Delta\mathrm{BIC} = \mathrm{BIC}_{\mathrm{Model1}} - \mathrm{BIC}_{\mathrm{Model2}}. \tag{37}$$

We adopt criteria proposed by Kass & Raftery (1995), such that $\Delta\mathrm{BIC} > 6$ indicates a strong preference for Model 2 over Model 1. Conversely, if $\Delta\mathrm{BIC} < -6$, there is a strong preference for Model 1 over Model 2. In cases where $-6 < \Delta\mathrm{BIC} < 6$, no strong preference is suggested for either model.

Figure 1 shows that FDM and SIDM models are favored over the NFW model, as evidenced by the 25th, 50th, and 75th percentiles of the ΔBIC values: 1.24, 10.98, and 24.62 for FDM and 4.91, 11.28, and 23.06 for SIDM, respectively. Notably, SIDM appears to have a slight preference over FDM, with the 25th, 50th, and 75th percentile ΔBIC values of 2.83, 3.05, and 5.18. In addition, we also tested the FDM model with a fixed $\log m_{22} = 1$ and found that its performance is similar to when $\log m_{22}$ is treated as a free parameter. In both cases, the FDM model consistently outperforms the NFW profile in terms of BIC.

While the preference for SIDM is not overwhelmingly large, it is worth considering that two galaxies poorly fit the SIDM model and skew the ΔBIC distribution toward FDM. Excluding these two galaxies would shift the preference to the SIDM model. Overall, these results demonstrate that both FDM and SIDM models provide better fits for rotation curves compared to the NFW model. Furthermore, the SIDM model offers a comparatively efficient fit, involving fewer parameters than the FDM model.

The comparison between FDM and SIDM models reveals significant differences, particularly regarding the characteristics of dark matter cores and transition radii. While both models exhibit similar core sizes, the transition radius in the SIDM halo is notably located much further out than in the FDM halo. This discrepancy is particularly evident in certain galaxies, such as UGC 07524 (see Figure 2). In 20 out of 38 galaxies, the transition radius extends even beyond the range of rotation curve data points, indicating that the dark matter component in those galaxies can be effectively described by a pure isothermal halo, similar to findings by Loizeau & Farrar (2021). The larger transition radius observed in the SIDM halo can be attributed to the mass continuity requirement, which prevents abrupt transitions characteristic of the FDM model. Additionally, the SIDM profile incorporates the effects of the baryonic potential, which influences the distribution of dark matter.

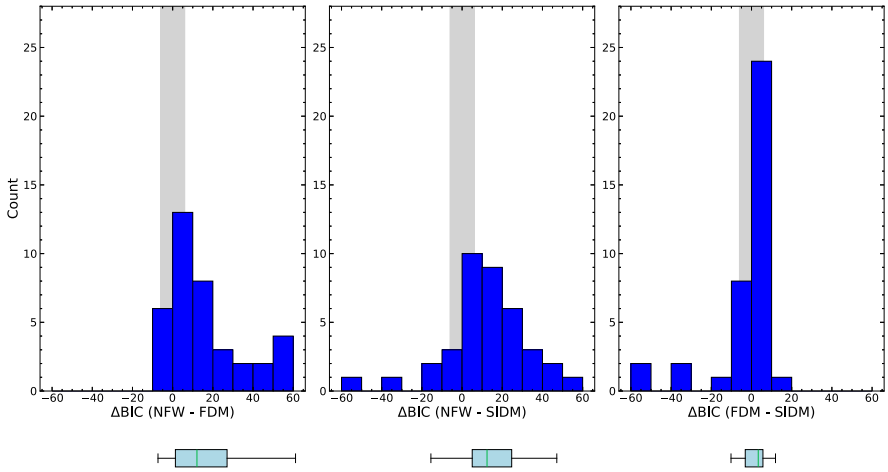

Figure 1. ΔBIC values between models. Positive values indicate a preference for the second model in the subplots and vice versa. The vertical gray band shows the range of ΔBIC where the preference for either model is not strong. Below each panel, the colored box and whisker summarize the spread of the corresponding histogram. The box extends from the first to the third quartile of ΔBIC values, with the median indicated by the vertical green line. The whiskers extend a factor of 1.5 times the interquartile range.

It is generally expected that a strong baryonic potential, particularly one with a centralized distribution, would typically result in a more compact core with a smaller transition radius. However, in the case of dwarf galaxies, the situation is different. Here, the dominance of dark matter leads to larger core sizes (Kaplinghat et al. 2014; Elbert et al. 2016), and the transition radius is found at significantly greater distances. This phenomenon highlights the complex interplay between baryonic and dark matter components in these systems.

4.2. Concentration–Mass Relation

4.2.1. NFW

The relation between concentration and virial mass parameters of NFW haloes has been derived from the evolution of relaxed halo structures. In the context of Planck cosmology (Planck Collaboration 2014), simulations conducted by Dutton & Macciò (2014) include haloes of $M_{200} = 10^{10}$–$10^{15}\,M_{\odot}$ (covering dwarf galaxies to galaxy clusters). These simulations yield a simple formula for the concentration–mass relation of NFW haloes (see Equation (4) for redshift $z = 0$), which agrees well with observed halo concentrations and masses of spiral galaxies, groups, and clusters of galaxies at low redshift.

We adopt C_{200} and V_{200} as fitting parameters, deriving M_{200} from these values. In our rotation curve analysis using the NFW model, most galaxies exhibit notably lower C_{200} and higher V_{200} values than predicted by simulations. Consequently, the derived M_{200} values are often unreasonably high and physically inconsistent. When the concentration–mass relation is set as a prior in the fittings, the NFW model generally fails to reproduce the observed rotation curves of most dwarf galaxies in our sample. This constraint leads to poorer fits compared to those achieved without enforcing the relation. These findings underscore the NFW model's limitations in accurately fitting the rotation curves of dwarf galaxies.

Figure 3 shows the results obtained from rotation curve fittings without applying the concentration–mass relation. Also shown in the figure is the concentration–mass relation extended downward to $M_{200} = 10^{8} M_{\odot}$, assuming the relation remains valid well below the mass range explored by simulations in Dutton & Macciò (2014). The rotation curve fittings for most galaxies give significantly lower C_{200} values than those predicted by simulations, while the M_{200} values appear excessively large for dwarf galaxies, likely indicating unrealistic outcomes. Among the galaxies in our study, only three favor the NFW model and show marginal agreement with the concentration–mass relation; conversely, those that adhere to this relation predominantly reject the NFW model.

It is crucial to note that while the concentration–mass relation at $z = 0$ can be expressed in the general form

$$\log_{10}(C_{200}) = a - b \log_{10}(M_{200}/[10^{12} h^{-1} M_{\odot}]), \qquad (38)$$

parameter values a and b vary across different cosmological simulations, reflecting diverse initial conditions and free parameters. Moreover, the simulations predominantly focus on more massive haloes, often overlooking baryonic effects that considerably influence inner halo parameters. Incorporating baryonic physics can lead to denser halo profiles, potentially enhancing dark matter halo concentrations by up to 30% at galaxy scales (Duffy et al. 2010).

4.2.2. FDM

The fittings using the FDM model are performed in two ways: first, by incorporating concentration–mass relation as a

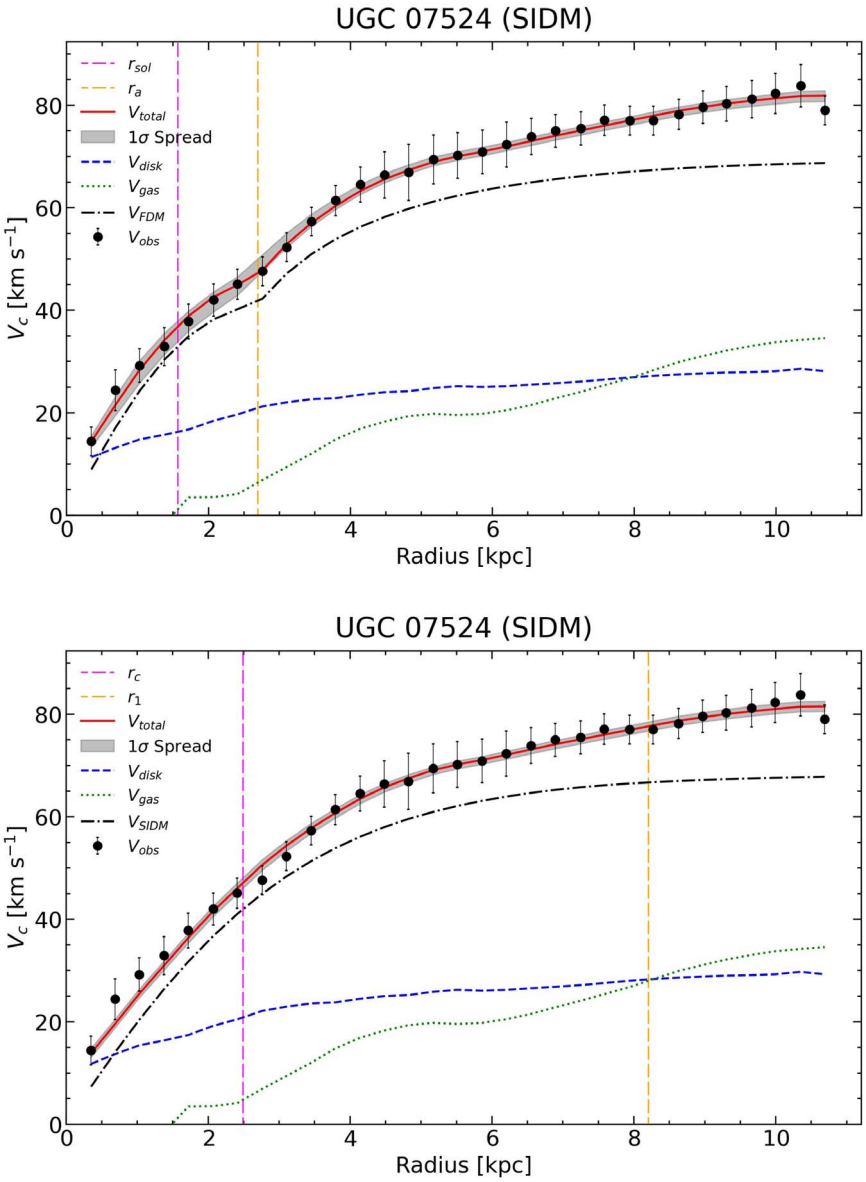

Figure 2. Decompositions of the UGC 07524 rotation curve using FDM and SIDM halo models. The pink and orange vertical dashed lines respectively show the core radius and the transition radius for each model.

prior, referred to as FDMc, and second, by excluding this prior, denoted simply as FDM. The concentration–mass relation was derived by Dentler et al. (2022) from simulations of the FDM power spectrum and halo mass function. These simulations reveal a characteristic flat feature in the density profile of the FDM halo that is not confined only to the core region but extends into the NFW "tail" at larger radii. This feature results in a lower concentration parameter compared to that of the NFW halo, necessitating a modification of the concentration–mass relation at lower mass scales as shown in Equation (18). Unlike the NFW model, we observe no notable difference in the fitting quality when the concentration–mass relation is incorporated as a prior or when it is excluded. With more parameters, the FDM model offers considerably more flexibility, enabling it to adjust to other parameter values while still achieving a good fit to the observational data. In addition, the FDM model fits the observed rotation curves better compared to the NFW model. Therefore, we will utilize FDMc for further analysis.

The concentration–mass relation of the FDM halo is influenced by the characteristic parameter of the model, specifically the FDM particle mass ($\log m_{22}$). Galaxies in our

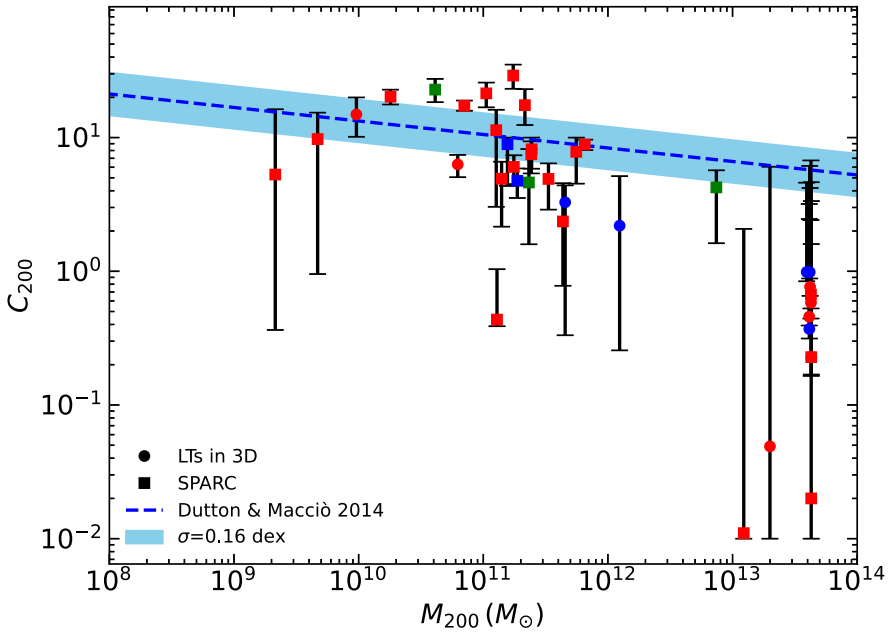

Figure 3. Comparison between concentration–mass relation from simulations by Dutton & Macciò (2014) with 0.16 dex scatter and our results based on rotation curve fittings using the NFW halo model. Green, blue, and red markers indicate galaxies that support, show no preference, and reject the NFW model, respectively. Not imposing the concentration–mass relation results in unrealistically large M_{200} values.

sample exhibit different best fits of particle mass, as shown in Figure 4. We can see that many of the 95% credible intervals for the mass parameter of the individual galaxies are in tension with each other. However, to establish a representative value of $\log m_{22}$ for the entire sample, we utilize the median of the FDM particle mass values derived from the galaxy sample, $\log m_{22} = 0.136$. All galaxies in Figure 4 lie within 2σ from this median value.

Without applying the concentration–mass relation, the FDM model produces too high C_{200} values, deviating from the expected relation suggested by Dentler et al. (2022) for the median value of $\log m_{22}$ (see Figure 5). Without constraining C_{200}, the parameters can assume any value within the prior range, as long as the density profile remains continuous at the transition radius, resulting in the large scatter in the values of C_{200}. The C_{200} values of most galaxies even lie above the concentration–mass relation for a $\log m_{22}$ value that is 1σ above the median.

4.3. Dark Matter Core

Unlike the NFW model which exhibits a cuspy density profile, the central regions of FDM and SIDM haloes are modified due to the properties and interactions of dark matter that result in the formation of cores. In the FDM model, the superposition of particle waves leads to the formation of soliton cores that vary in size from galaxy to galaxy and are coupled with the halo size through the soliton-halo mass relation (Schive et al. 2014a, 2014b). The SIDM model predicts formations of core structures induced by non-gravitational self-interactions that allow the dark matter to smooth out the central density, avoiding the cuspy density profiles predicted by CDM models.

We expect that dark matter interacts at least gravitationally with baryonic matter. To better understand how these two components coexist and influence the structure and dynamics of galactic systems, we explore the correlation between the core radius of dark matter and the effective radius of stellar distribution. These two radii serve as indicators of the spatial distribution of dark matter and baryonic matter within galaxies. The dark matter core radius refers to the size of the central region of any given galaxy wherein the dark matter density is relatively flat or constant. The stellar effective radius of a galaxy is defined as the radius within which half of the total stellar light (or mass) of the galaxy is contained. It characterizes the size and structure of the galaxy and helps in comparing different types of galaxies. Correlation between the core radius and the effective radius gives us clues on how dark matter properties relate to the structure of galaxies, especially in their central regions, and possible processes involved in the formation and evolution of galaxies.

Figure 6 shows a notable direct proportionality between the effective radius, $r_{\rm eff}$, and the soliton core radius, $r_{\rm sol}$, of the galaxies in our sample, evidenced by a Pearson correlation coefficient of 0.76. This correlation likely arises from the

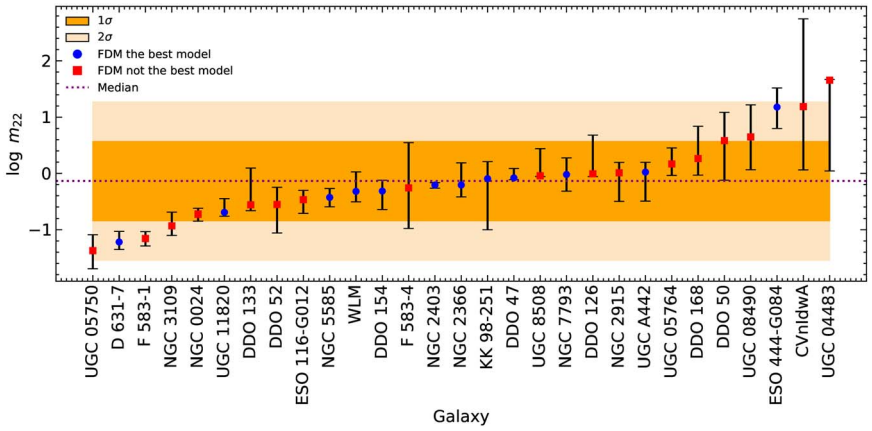

Figure 4. MAP and 95% credible intervals of the parameter log m_{22} from fitting the rotation curve of the individual galaxy using the FDM halo model. Only galaxies that do not reject the FDM model are included. The dotted line indicates the median value, log $m_{22} = -0.136$ or $m_{\rm FDM} = 0.731 \times 10^{-22}$ eV, while the shaded regions represent 1σ and 2σ standard deviations.

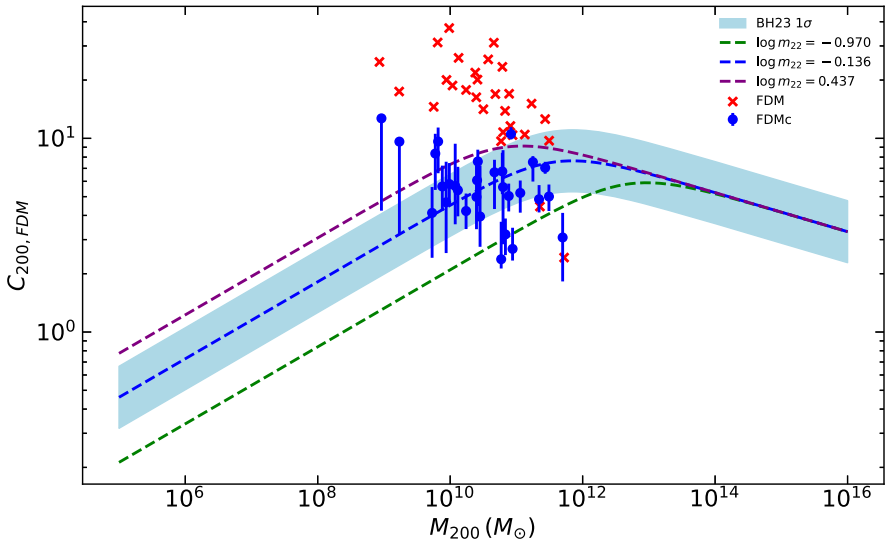

Figure 5. Comparison of C_{200} and M_{200} values obtained from rotation curve fitting using the FDM model with and without applying the concentration–mass relation. The reference concentration–mass relation suggested by Dentler et al. (2022) is shown as a blue dashed line with a scatter of 0.16 dex for log $m_{22} = 0.136$, and the median of log m_{22} shown in Figure 4. The purple and green dashed lines represent the relation for log $m_{22} = -0.937$ and 0.437 ($\pm 1\sigma$ from the median of log m_{22}) respectively.

gravitational interaction between dark matter and baryonic matter. Baryons residing within the FDM halo play a significant role in the growth of the soliton core, contributing to its increased mass and compactness (Bar et al. 2018). However, this relation is complex and influenced by multiple factors, such as the inverse proportionality between FDM particle mass and soliton size (see Equations (7) and (8)), and the relative contribution of baryons and dark matter within the soliton region. Unfortunately, our study cannot discern the influence of the latter factor since the majority of our sample are dark matter-dominated dwarf galaxies.

We define the SIDM core radius as the radius at which the density drops to half the central density, consistent with the definition used by various authors (Rocha et al. 2013; Zavala et al. 2013; Kaplinghat et al. 2014). Figure 7 indicates a notable linear relation between the effective radius, $r_{\rm eff}$, and the SIDM core radius, r_c, of the galaxies in our sample, as shown by a Pearson correlation coefficient of 0.7. This correlation most likely arises from the self-interactions of SIDM particles, which allow them to move and redistribute in response to the baryonic potential more effectively than CDM, leading to coupled evolution between the baryonic and dark matter components

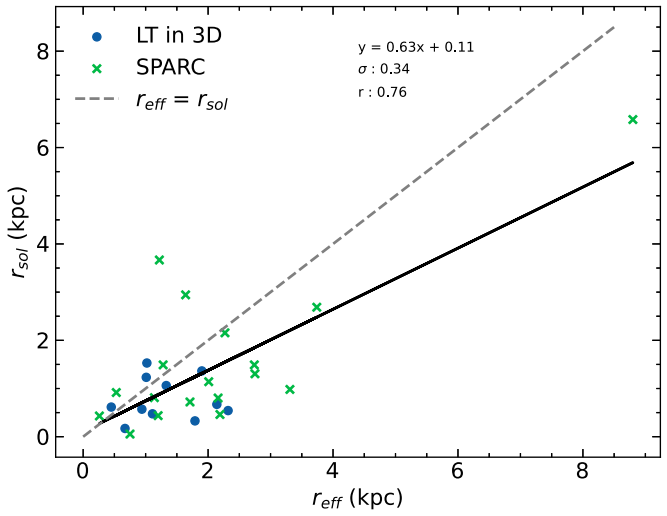

Figure 6. Relation between the effective radius and the soliton core radius in the FDM model. The solid black line represents a linear relation between the two radii, while the dashed gray line represents $r_{\rm eff} = r_{\rm sol}$. To ensure the validity of the core radius values, only values from galaxies that do not reject the FDM model based on the BIC criterion are included.

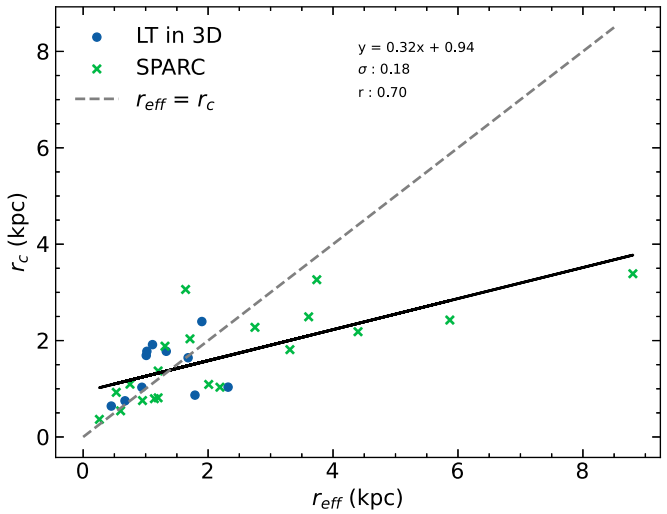

Figure 7. Relation between the effective radius and isothermal core radius in the SIDM model. The solid black line represents the linear relation between the two radii, while the dashed gray line represents $r_{\rm eff} = r_c$. To ensure the validity of the core radius values, only values from galaxies that do not reject the SIDM model based on the BIC criterion are included.

(Kaplinghat et al. 2014; Vogelsberger et al. 2014). In dark matter-dominated dwarf galaxies like those studied here, thermalization results in large isothermal cores, whereby baryons respond by forming a more extended stellar distribution. However, similar to the FDM model, this relationship is complex and influenced by several factors, including the SIDM particle scattering rate within the isothermal core, the cross-section per unit mass of SIDM particles (σ/m_χ), and the dominant matter fraction at the inner radius. Nonetheless, the effects of these factors are not apparent in this work due to our assumption of a constant σ/m_χ and the predominance of dark matter-rich dwarf galaxies in our sample.

4.4. Dark Matter Fraction

We evaluate dark matter fractions, f, at two characteristic radii: at the effective radius ($r_{\rm eff}$) and at the optical radius ($r_{\rm opt} = 3.2r_d$), where r_d is the scale radius (or scale length) of the disk. It is generally expected that dark matter becomes increasingly dominant at the outer radius of galaxies. So, it is anticipated that $f_{\rm opt} > f_{\rm eff}$. Figure 8 reveals that FDM and SIDM models exhibit a greater variation of dark matter fractions relative to the NFW model. This reflects the ability of the FDM and SIDM haloes to conform to different shapes of rotation curves and dark matter distributions of the diverse observed rotation curves.

The difference in the dark matter fractions between the three models is expected due to the different characteristics of the dark matter distributions in these models. The NFW model features a cuspy density profile, meaning the dark matter density increases steeply toward the center of the halo. As a result, the dark matter fraction is already high at the inner radius (closer to the galaxy's center) and does not change significantly between the inner and outer radii. This is in contrast to the FDM halo, which has a soliton core with a constant density that affects the dark matter fraction at the inner radius, and the fraction increases after the transition radius to the NFW profile (Khelashvili et al. 2023). The fraction can increase significantly from the effective to the optical radii if the transition radius is located between the two of them.

Meanwhile, despite the existence of the dark matter core, the SIDM halo shows little change in the dark matter fraction up to the outer radius, and the fraction is generally high even in the inner part of the halo where the constant density core resides. This behavior is markedly different from the FDM model since the transition occurs smoothly at a significantly larger radius in the SIDM model, resulting in an insignificant change in the fraction at the inner radius. It is important to note that we use a spherical approximation of baryons for the SIDM case, which differs from the approach used in the other models. However, Ren et al. (2019) suggest that this approximation should agree with the disk approximation within 10%–20%. Therefore, while some variance in the dark matter fraction between the two methods is expected, the trend should be very similar in general.

Some galaxies show $f_{\rm eff} > f_{\rm opt}$, which may be caused by variations in the baryon distribution due to galaxy morphology or external perturbations. Some galaxies in the sample are dwarf irregulars, which may possess local features that can affect the velocity at specific radii, thereby altering the fraction

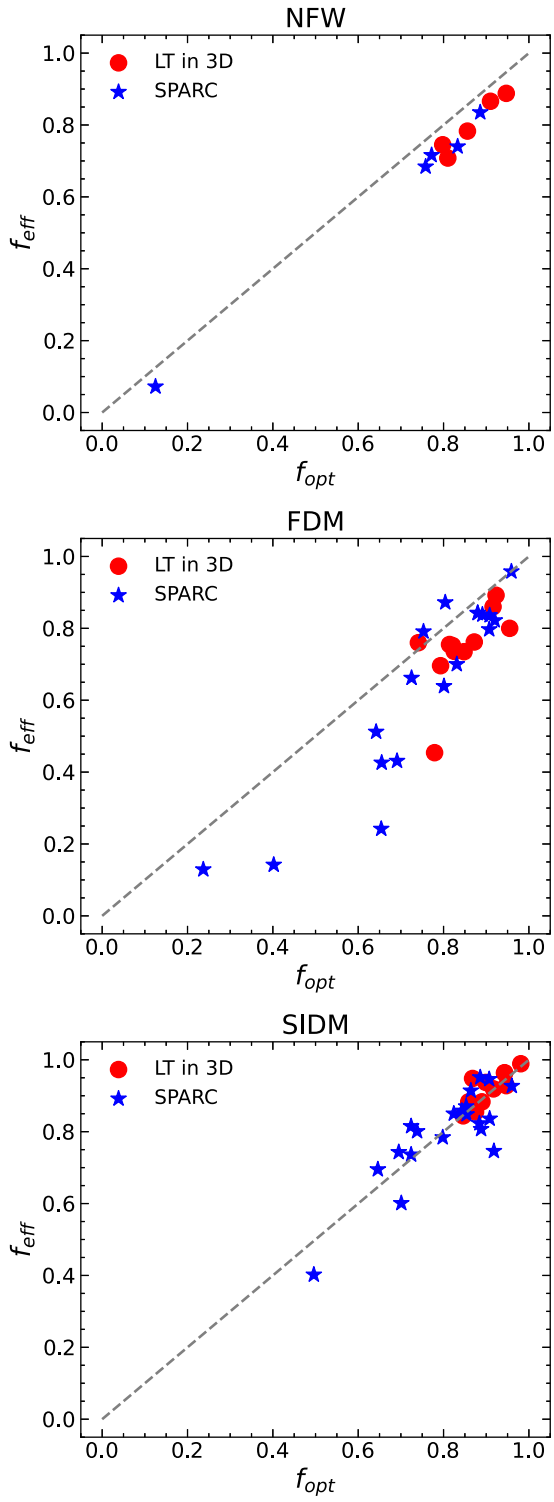

Figure 8. Comparison of the dark matter fractions at the effective and optical radii, from top to bottom respectively, for NFW, FDM, and SIDM haloes. The dashed gray line represents $f_{\rm eff} = f_{\rm opt}$. To ensure the validity of the fraction values, only values from galaxies that do not reject the corresponding model based on the BIC criterion are included.

values used in the calculation involving interpolations. The low mass and shallow gravitational potential wells of dwarf galaxies are also sensitive to internal and external perturbations that can change the distribution of matter, especially baryons. Ejections and strippings of the baryonic component from gas-rich dwarf irregular galaxies can significantly decrease their central density (Arraki et al. 2012). This effect is crucial especially for LT in 3D galaxies, which are members of the Local Group and often experience gravitational interactions with massive galaxies like the Milky Way and Andromeda.

5. Discussion

Applying the NFW concentration–mass relation often leads to a poor fit between the model and the observational data. On the other hand, not adhering to the relation tends to yield an NFW model that better fits the data but results in implausible parameter values for many galaxies. For instance, some fits produce extremely low C_{200} values (<1), and very high V_{200} values ($>200\,{\rm km\ s^{-1}}$), atypical for dwarf galaxies. These unrealistic parameter values result in estimates on the order of hundreds of kpc for the derived virial and NFW scale radii, and virial masses of $M_{200} > 10^{13} M_{\odot}$, unrealistic for dwarf galaxies.

A similar issue was identified by Haghi et al. (2018), who attempted to reproduce the concentration–mass relation using SPARC rotation curves and found a significantly steeper relation than what cosmological simulations predicted. They observed higher concentrations in low-mass galaxies, whereas more massive galaxies showed the opposite trend. In contrast, our study does not reveal such a trend; instead, most of our findings fall below predictions by simulations. This discrepancy may be attributed to our exclusive focus on dwarf galaxies with a narrow mass range, whereas Haghi et al. (2018) analyzed a broader range of galaxies within the SPARC sample.

There are several potential explanations for this issue. First, the concentration–mass relation used may not be universally applicable, particularly since it is derived from dark-matter-only simulations and does not account for baryons or other physical processes that can alter the distribution of matter in the halo. Second, the NFW model may not adequately fit the sample of dwarf galaxies, as indicated by its generally poorer performance than the other two models. Third, some of the rotation curves in our sample might not yet reach the flat region, meaning that not all mass has been fully accounted for. This could lead to problems when using the concentration–mass relation, as it assumes that in every galaxy the rotation curve already flattens, making the NFW model a poor fit for the data.

The FDM model, despite fitting the data better, encounters similar issues. To apply the FDM concentration–mass relation, we assume that the CDM concentration–mass relation follows

the power law in Equation (4). However, several studies (Bosch et al. 2014; Correa et al. 2015; Diemer & Kravtsov 2015) have observed that this relation tends to flatten at lower masses and low redshifts, which may be attributed to the varying dynamical states of the simulated dark matter haloes. In addition, the concentration–mass relation for FDM depends on at least two parameters: the particle mass and the concentration parameter of CDM (see Equation (4)). Observations have yet to converge to a single value for the FDM particle mass (Bañares-Hernández et al. 2023; Khelashvili et al. 2023), and we identify a tension of more than 2σ in the best-fit particle mass values for certain galaxies (see Figure 4). Another critical factor is the influence of various physical processes within galaxies, such as mergers, baryonic feedback, or distortions caused by neighboring massive objects, which can significantly affect dark matter halo concentrations.

As discussed in Section 4.2, the SIDM model predicts significantly larger transition radii, often extending beyond the range of the observed rotation curve data (see Figure 2). The extensive cores and transition radii are primarily influenced by the choice of σ/m_χ. In this study, we adopt a velocity-independent cross-section of 3 $\mathrm{cm}^2\ \mathrm{g}^{-1}$, a value consistent with previous research and well-suited for modeling interactions at galaxy scales (see Section 3). Increasing σ/m_χ results in less dense and more extended cores, whereas decreasing it leads to denser and more compact cores.

The dark matter fraction at the characteristic radius has several limitations as a representation of the dark matter distribution for several reasons. First, interpolating the data to estimate the rotational velocity at this characteristic radius can introduce inaccuracies. Second, spiral arms and other structural features of galaxies cause local variations that may not accurately reflect the overall dark matter distribution. Third, determining the characteristic radius of galaxies relies on assumptions derived from the disks of nearby galaxies, meaning that different models or fitting methods can yield varying characteristic radius values (Freeman 1970; Sharma et al. 2021). Fourth, the assumption of a spherically symmetric dark matter halo may not hold for all galaxies, as many exhibit triaxiality due to dynamic processes during their formation and evolution (Despali et al. 2014). Finally, neglecting uncertainties in galaxy distances and inclinations can lead to inaccuracies in the radial distances of rotation curves and the baryonic masses of galaxies (Li et al. 2018). In cosmological simulations, these limitations do not occur because the modeling comprehensively tracks the evolution of dark matter and baryons. This approach yields a more accurate distribution of dark matter without involving data interpolation. Furthermore, in the simulations, quantities such as characteristic radius, distance, and inclination of galaxies are precisely calculated so that no uncertainties affect the resulting rotation curves and baryon masses.

6. Conclusions

In this study, we investigated three dark matter models: NFW (representing standard CDM), FDM, and SIDM. We utilized rotation curve data of dwarf galaxies from SPARC (Lelli et al. 2016) and LT in 3D (Iorio et al. 2017) catalogs. Our findings indicate significant discrepancies between the concentration–mass relations predicted by simulations of the NFW and FDM models and those derived from the rotation curve fitting of observed dwarf galaxies.

A notable finding is the positive correlation between the effective radius and the soliton core radius within the FDM model. This suggests that gravitational interactions between dark matter and baryons play a critical role in shaping the correlation. Additionally, factors such as the FDM particle mass contribute to this correlation. In the SIDM model, core sizes also correlate with the effective radius, primarily influenced by thermalization processes within the dark matter halo.

Our study emphasizes the variations in dark matter distribution among different models, particularly highlighting that the FDM and SIDM models demonstrate a broader range of distributions than the NFW model. This increased diversity indicates that FDM and SIDM may provide a more accurate representation of the diverse rotation curves and dark matter distributions observed in galaxies.

We underscore the necessity of utilizing more extensive galaxy catalogs to effectively capture the diverse properties of dark matter haloes. Future research should focus on refining the concentration–mass relation, integrating baryonic effects, and enhancing fitting techniques. These efforts will contribute to a more profound understanding of the intricate nature of dark matter within galaxies.

Acknowledgments

We thank Institut Teknologi Bandung for financially supporting this research through PPMI KK 2024 Program, contract number 616BO/IT1.C02/KU/2024.

References

Andrae, R., Schulze-Hartung, T., & Melchior, P. 2010, arXiv:1012.3754
Angulo, R. E., & Hahn, O. 2022, LRCA, 8, 1
Arraki, K., Klypin, A., More, S., & Trujillo-Gomez, S. 2012, MNRAS, 438, 1466
Bañares-Hernández, A., Castillo, A., Martin Camalich, J., & Iorio, G. 2023, A&A, 676, A63
Bar, N., Blas, D., Blum, K., & Sibiryakov, S. 2018, PhRvD, 98, 083027
Bar, N., Blum, K., & Sun, C. 2022, PhRvD, 105, 083015
Benítez-Llambay, A., Frenk, C. S., Ludlow, A. D., & Navarro, J. F. 2019, MNRAS, 488, 2387
Bennett, C. L., Larson, D., Weiland, J. L., et al. 2013, ApJS, 208, 20
Bernal, T., Fernández-Hernández, L. M., Matos, T., & Rodríguez-Meza, M. A. 2018, MNRAS, 475, 1447
Bosch, F. C. v. d., Jiang, F., Hearin, A., et al. 2014, MNRAS, 445, 1713
Bullock, J. S., & Boylan-Kolchin, M. 2017, ARA&A, 55, 343
Correa, C. A. 2023, ScPPP, 12, 59

Correa, C. A., Wyithe, J. S. B., Schaye, J., & Duffy, A. R. 2015, MNRAS, 452, 1217
Creasey, P., Sameie, O., Sales, L. V., et al. 2017, MNRAS, 468, 2283
de Martino, I., Chakrabarty, S. S., Cesare, V., et al. 2020, Univ, 6, 107
Del Popolo, A., Le Delliou, M., & Lee, X. 2018, Galax, 6, 67
Dentler, M., Marsh, D. J. E., Hložek, R., et al. 2022, MNRAS, 515, 5646
Despali, G., Giocoli, C., & Tormen, G. 2014, MNRAS, 443, 3208
Despali, G., Sparre, M., Vegetti, S., et al. 2019, MNRAS, 484, 4563
Di Cintio, A., Brook, C. B., Dutton, A. A., et al. 2014, MNRAS, 441, 2986
Di Teodoro, E. M., & Fraternali, F. 2015, MNRAS, 451, 3021
Diemer, B., & Kravtsov, A. V. 2015, ApJ, 799, 108
Duffy, A., Schaye, J., Kay, S., et al. 2010, MNRAS, 405, 2161
Dutton, A. A., & Macciò, A. V. 2014, MNRAS, 441, 3359
Elbert, O. D., Bullock, J., Kaplinghat, M., et al. 2018, ApJ, 853, 109
Ferreira, E. G. M. 2021, A&ARv, 29, 7
Flores, R. A., & Primack, J. R. 1994, ApJL, 427, L1
Foreman-Mackey, D., Hogg, D. W., Lang, D., & Goodman, J. 2013, PASP, 125, 306
Freeman, K. C. 1970, ApJ, 160, 811
Goodman, J., & Weare, J. 2010, CAMCS, 5, 65
Haghi, H., Khodadadi, A., Ghari, A., Zonoozi, A. H., & Kroupa, P. 2018, MNRAS, 477, 4187
Hu, W., Barkana, R., & Gruzinov, A. 2000, PhRvL, 85, 1158
Hui, L., Ostriker, J. P., Tremaine, S., & Witten, E. 2017, PhRvD, 95, 043541
Iorio, G., Fraternali, F., Nipoti, C., et al. 2017, MNRAS, 466, 4159
Kamada, A., Kaplinghat, M., Pace, A. B., & Yu, H.-B. 2017, PhRvL, 119, 111102
Kaplinghat, M., Keeley, R. E., Linden, T., & Yu, H.-B. 2014, PhRvL, 113, 021302
Kaplinghat, M., Ren, T., & Yu, H.-B. 2020, JCAP, 2020, 027
Kaplinghat, M., Tulin, S., & Yu, H.-B. 2016, PhRvL, 116, 041302
Karttunen, H., Kröger, P., Oja, H., Poutanen, M., & Donner, K. J. 2017, Fundamental Astronomy (Berlin: Springer)
Kass, R. E., & Raftery, A. E. 1995, JASA, 90, 773
Khelashvili, M., Rudakovskyi, A., & Hossenfelder, S. 2023, MNRAS, 523, 3393
Klypin, A., Kravtsov, A. V., Valenzuela, O., & Prada, F. 1999, ApJ, 522, 82
Lelli, F., McGaugh, S. S., & Schombert, J. M. 2016, AJ, 152, 157
Li, P., Lelli, F., McGaugh, S., & Schombert, J. 2018, A&A, 615, A3
Li, P., Lelli, F., McGaugh, S., & Schombert, J. 2020, ApJS, 247, 31
Loizeau, N., & Farrar, G. R. 2021, ApJL, 920, L10
Marsh, D. J. E., & Pop, A.-R. 2015, MNRAS, 451, 2479
Matos, T., & Arturo Ureña-López, L. 2001, PhRvD, 63, 063506
May, S., & Springel, V. 2021, MNRAS, 506, 2603
Mina, M., Mota, D. F., & Winther, H. A. 2022, A&A, 662, A29
Mocz, P., Fialkov, A., Vogelsberger, M., et al. 2019, PhRvL, 123, 141301
Moore, B. 1994, Natur, 370, 629
Moore, B., Ghigna, S., Governato, F., et al. 1999, ApJL, 524, L19
Navarro, J. F., Eke, V. R., & Frenk, C. S. 1996, MNRAS, 283, L72
Navarro, J. F., Frenk, C. S., & White, S. D. M. 1996, ApJ, 462, 563
Navarro, J. F., Frenk, C. S., & White, S. D. M. 1997, ApJ, 490, 493
Oh, S.-H., Hunter, D. A., Brinks, E., et al. 2015, AJ, 149, 180
Oman, K. A., Navarro, J. F., Fattahi, A., et al. 2015, MNRAS, 452, 3650
Persic, M., & Salucci, P. 1990, MNRAS, 247, 349
Persic, M., Salucci, P., & Stel, F. 1996, MNRAS, 281, 27
Planck Collaboration 2014, A&A, 571, A16
Planck Collaboration 2020, A&A, 641, A6
Pontzen, A., & Governato, F. 2012, MNRAS, 421, 3464
Read, J. I., Iorio, G., Agertz, O., & Fraternali, F. 2017, MNRAS, 467, 2019
Ren, T., Kwa, A., Kaplinghat, M., & Yu, H.-B. 2019, PhRvX, 9, 031020
Rocha, M., Peter, A. H. G., Bullock, J. S., et al. 2013, MNRAS, 430, 81
Rubin, V. C., & Ford, W. K., Jr., 1970, ApJ, 159, 379
Rubin, V. C., Ford, W. K., Jr., & Thonnard, N. 1978, ApJL, 225, L107
Sagunski, L., Gad-Nasr, S., Colquhoun, B., Robertson, A., & Tulin, S. 2021, JCAP, 2021, 024
Sales, L. V., Wetzel, A., & Fattahi, A. 2022, NatAs, 6, 897
Santos-Santos, I. M. E., Navarro, J. F., Robertson, A., et al. 2020, MNRAS, 495, 58
Schive, H.-Y., Chiueh, T., & Broadhurst, T. 2014a, NatPh, 10, 496
Schive, H.-Y., Liao, M.-H., Woo, T.-P., et al. 2014b, PhRvL, 113, 261302
Sharma, G., Salucci, P., & van de Ven, G. 2021, A&A, 653, A20
Sofue, Y., Tutui, Y., Honma, M., et al. 1999, ApJ, 523, 136
Spergel, D. N., & Steinhardt, P. J. 2000, PhRvL, 84, 3760
Springel, V., White, S. D. M., Jenkins, A., et al. 2005, Natur, 435, 629
Tollet, E., Macciò, A. V., Dutton, A. A., et al. 2016, MNRAS, 456, 3542
Tulin, S., & Yu, H.-B. 2018, PhR, 730, 1
Veltmaat, J., Niemeyer, J. C., & Schwabe, B. 2018, PhRvD, 98, 043509
Vogelsberger, M., Zavala, J., Simpson, C., & Jenkins, A. 2014, MNRAS, 444, 3684
Zavala, J., Vogelsberger, M., & Walker, M. G. 2013, MNRAS, 431, L20
Zentner, A., Dandavate, S., Slone, O., & Lisanti, M. 2022, JCAP, 2022, 031